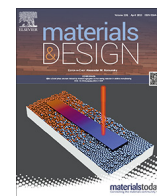




Contents lists available at ScienceDirect

Materials &amp; Design

journal homepage: [www.elsevier.com/locate/matdes](http://www.elsevier.com/locate/matdes)

# Influence of ECAP process on mechanical, corrosion and bacterial properties of Zn-2Ag alloy for wound closure devices

García-Mintegui Claudia<sup>a,b,c</sup>, Goncharov Ivan<sup>d</sup>, Ortiz-Membrado Laia<sup>e</sup>, Jiménez-Piqué Emilio<sup>c,e</sup>, Ginebra Maria-Pau<sup>a,c,f</sup>, Vedani Maurizio<sup>d</sup>, Cortina José Luís<sup>b,c</sup>, Peguerols Marta<sup>a,c,\*</sup>

<sup>a</sup> Biomaterials, Biomechanics and Tissue Engineering Group, Department of Materials Science and Engineering, Universitat Politècnica de Catalunya (UPC), Barcelona East School of Engineering (EEBE), 08019 Barcelona, Spain

<sup>b</sup> Resource Recovery and Environmental Management Group, UPC, EEBE, 08019 Barcelona, Spain

<sup>c</sup> Barcelona Research Center in Multiscale Science and Engineering, UPC, EEBE, 08019 Barcelona, Spain

<sup>d</sup> Department of Mechanical Engineering, Politecnico di Milano, 20156 Milan, Italy

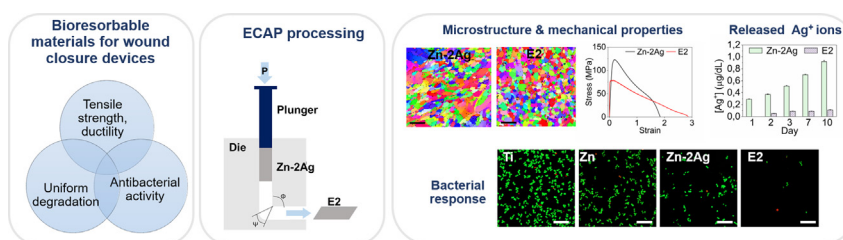
<sup>e</sup> Structural Integrity, Micromechanics and Reliability of Materials Group, Department of Materials Science and Engineering, UPC, EEBE, 08019 Barcelona, Spain

<sup>f</sup> Institute for Bioengineering of Catalonia (IBEC), 08028 Barcelona, Spain

## HIGHLIGHTS

- Two ECAP cycles were applied to Zn-2Ag obtaining an ultra-fine-grained structure.
- Isotropic nanoscale mechanical properties were obtained after ECAP.
- The addition of Ag as alloying element in Zn reduced bacterial attachment.
- ECAP processed Zn-2Ag alloy showed excellent antibacterial effect for *S. Aureus*.
- ECAP processed Zn-2Ag alloy displayed uniformly degraded surface and corrosion rate.

## GRAPHICAL ABSTRACT



## ARTICLE INFO

### Article history:

Received 21 September 2022

Revised 2 February 2023

Accepted 9 March 2023

Available online 11 March 2023

### Keywords:

Binary alloys

Biomaterials

Equal channel angular pressing

Nanoindentation

Ultrafine-grained materials

Zinc alloys

## ABSTRACT

Actual polymeric wound closure devices are not optimal for load-bearing applications due to the low mechanical properties and the risk of inflammation and bacterial infection mainly produced by multifilament and braided configurations. Biodegradable metallic Zn alloys are promising materials candidates; however, mechanical performance, corrosion behaviour, and biological response should be controlled in order to inhibit the risk of inflammation and bacterial infection. To this end, a Zn-2Ag (2 wt% Ag) alloy was processed by ECAP to evaluate the concurrent combined effect of grain refinement and Ag alloying on biodegradation and antibacterial activity. Two ECAP cycles were successfully applied to a Zn-2Ag alloy obtaining a homogeneous ultra-fine-grained structure in which nanoindentation maps suggested isotropic mechanical properties. Lower UTS and YS with higher elongation was reported after ECAP with similar corrosion rates as before processing. ECAP processed samples showed a homogeneous Ag<sup>+</sup> release below the minimum inhibitory concentration for *S. Aureus* and no antibacterial effect was observed by diffusion. As expected, the presence of Ag in Zn-Ag alloys reduced bacterial attachment. Nevertheless, ECAP

\* Corresponding author at: Universitat Politècnica de Catalunya, Barcelona East School of Engineering, Department of Materials Science and Engineering, Av. Eduard Maristany, 10-14, 08019 Barcelona, Spain

E-mail addresses: [claudia.garcia.mintegui@upc.edu](mailto:claudia.garcia.mintegui@upc.edu) (G.-M. Claudia), [ivan.goncharov@polimi.it](mailto:ivan.goncharov@polimi.it) (G. Ivan), [laia.ortiz@upc.edu](mailto:laia.ortiz@upc.edu) (O.-M. Laia), [emilio.jimenez@upc.edu](mailto:emilio.jimenez@upc.edu) (J.-P. Emilio), [maria.pau.ginebra@upc.edu](mailto:maria.pau.ginebra@upc.edu) (G. Maria-Pau), [maurizio.vedani@polimi.it](mailto:maurizio.vedani@polimi.it) (V. Maurizio), [jose.luis.cortina@upc.edu](mailto:jose.luis.cortina@upc.edu) (C. José Luís), [marta.peguerols@upc.edu](mailto:marta.peguerols@upc.edu) (P. Marta).

processed Zn-2Ag provided an excellent antibacterial activity after 3 h probably caused by the uniformly degraded and thus, non-stable, surface observed after bacterial adhesion.

© 2023 The Authors. Published by Elsevier Ltd. This is an open access article under the CC BY-NC-ND license (<http://creativecommons.org/licenses/by-nc-nd/4.0/>).

## 1. Introduction

Wound closure devices such as sutures and staples are designed to approximate the edges of the injury tissue until its healing. The device should promote rapid closure by applying proper tension to prevent infections, but excessive stress could lead to ischemia or tissue necrosis. The fundamental material requirements for sutures gather good knot tensile strength and security, proper ductility, and biocompatibility [1]. In the last decades, bioresorbable materials have attracted so much attention since they eliminate the need for second surgeries for removal and reduce the associated long-term risks [2].

Current biodegradable wound closure devices are polymer-based, usually containing polylactic acid (PLA) and polyglycolic acid (PGA) [3]. These biodegradable polymers are destined for soft tissue closures, whereas inert metals such as titanium (Ti) and stainless steel (SS) are located in load-bearing applications due to their better mechanical performance [1]. Other compositions based on nylon or polypropylene (PP) are used as non-resorbable polymeric sutures. Nevertheless, their insufficient mechanical properties require multifilament wires to provide an adequate tension. Multifilament and braided configurations increase the risk of inflammation and bacterial infection [4]. Thus, biodegradable metallic devices have been studied to better match the demand for biodegradation and higher mechanical strength. Most studies have been focused on magnesium (Mg), but the high corrosion rate, the release of hydrogen, and the lack of ductility are still themes of concern [5]. On the other hand, iron (Fe) offers exceptional mechanical properties, but the degradation rates are low and the degradation products accumulate onto the tissues [6]. Zinc (Zn) alloys arose as potential candidates for biodegradable implants due to their biocompatibility and degradation rate which is intermediate between that of Mg and Fe [7]. However, a detected drawback is its relatively weak mechanical properties compared to Mg and Fe. In that sense, a considerable number of publications have been devoted in recent years to improve the mechanical properties of Zn alloys for cardiovascular or orthopaedic applications [8–10]. However, few studies have been focused on Zn-based materials for wound-closure applications up to date [11]. Guo et al. [12] developed Zn wires of 3- and 0.3-mm diameters with good in vitro biocompatibility and knot feasibility, where the better mechanical performance was related to the most refined microstructure. So far, achieving the adequate mechanical performance, corrosion behaviour, and biological response of Zn-based alloys remains an open challenge. Research indicates that alloying Zn with different elements or manipulating and controlling the microstructure are effective methods to improve mechanical properties [13]. Nevertheless, these methods will also have and influence in biodegradation and biocompatibility that should also be tuned.

Mechanical anisotropy has been reported as one of the causes of implant failure since the stress is not well-distributed along with the material after its implantation [2]. In this regard, the mechanical properties of Zn are closely related to its texture [14]. Another crucial factor for maintaining implant stability is its uniform degradation. Localized corrosion could accumulate local stress and lead to the breaking of the implant. Severe plastic deformation (SPD) is widely used to produce bulk ultrafine-grained (UFG) materials by introducing extremely large strain during the deformation process.

Among them, equal channel angular pressing (ECAP) is an effective procedure to prepare UFG metals with excellent mechanical and corrosion properties [15,16] and to improve the biocompatibility of Mg alloys [17]. Concerning ECAP processing of Zn alloys different studies have been performed. The obtained mechanical toughening in Zn-Mg or Zn-Mn alloys has been attributed to grain refinement of the Zn-alloy matrix, as well as the fragmentation and refinement of the secondary phases [18]. However, mechanical strengthening is not obtained for every Zn-based conjugation. For instance, the ultimate tensile strength (UTS) and yield strength (YS) of Zn-Cu alloys dramatically decreased after ECAP, whereas superplastic behaviour was observed [19]. Nonetheless, the ECAP effect on bacterial response of Zn alloys has not yet been studied.

Surgical site infections (SSIs) are surgical-related infections related to wound closure interventions that appear within 30 days after implantation (or one year in the case of implants) [20]. Different factors affect the risk of bacterial incidences, such as the geometry of the implant or its composition. For instance, multifilament and braided sutures are more prone to infection because of the increased attachment of the bacteria within the structure [21]. Therefore, suture materials are loaded with antibiotics such as triclosan [22] or gentamicin [23]. However, the development of antibacterial resistance forces researchers to find alternatives to avoid SSI. *Staphylococcus aureus* (*S. aureus*) is present in most of the known SSIs and bloodstream infections. The development of bacterial resistance and the lack of equally effective alternatives complicates methicillin-resistant *S. aureus* (MRSA) treatment [24]. Antibacterial agents such as silver (Ag) nanoparticles have been included in the polymeric structures hindering possible infections [25]. Besides, the incorporation of metallic ions such as silver ( $\text{Ag}^+$ ), copper ( $\text{Cu}^{2+}$ ), and zinc ( $\text{Zn}^{2+}$ ), or the correspondent oxides ( $\text{AgO(s)}$ ,  $\text{CuO(s)}$ ,  $\text{ZnO(s)}$ ) to conventional titanium have been demonstrated to provide antibacterial properties to the implants [26].

This work aims to provide more insights into the mechanical effects of grain refinement in Zn-based alloys and evaluate its impact in bacterial performance. To this end, a Zn-2Ag (2 wt% Ag) alloy was processed and investigated to evaluate the achievable strengthening induced by grain refining by ECAP and the concurrent combined effect of grain refinement and Ag alloying on biodegradation and antibacterial activity.

## 2. Materials and methods

### 2.1. Materials and ECAP processing

Zn-2Ag (2 wt% Ag) metallic bar was provided by GoodFellow (UK). The as-received condition of the bars was extruded and cold rolled. Billets with 10 mm of diameter and 100 mm of length were machined from the starting material. The ECAP die was composed by two cylindrical channels intersecting at an angle of  $90^\circ$  with the outer arc of curvature of  $20^\circ$ . This geometry provides an equivalent plastic strain of 1.05 each pass according to Iwahashi equation [27]. Samples were pressed at room temperature with a speed of 5 mm/min using molybdenum disulphide ( $\text{MoS}_2$ ) as lubricant. Zn-2Ag billets were subjected up to two ECAP cycles. Second pressings were carried out by rotating the sample along its longitudinal axis by  $90^\circ$  before the second pass. Samples subjected to zero (as-received condition), one and two ECAP cycles were named as E0,

E1, and E2, respectively. Pressed samples were cut into 2.5 mm disks and grinded following metallographic standard procedures.

## 2.2. Microstructure characterization

The microstructure of the as-received and pressed samples after ECAP cycles were observed. To this end, the specimens were cut in the transversal and longitudinal direction, parallel to the direction of ECAP extrusion. The transversal and longitudinal sections were then abraded with silicon carbide grinding papers (grit size P800, P1200, and P2500, and polished using 6 and 3  $\mu\text{m}$  diamond suspension. Fine polishing was achieved using 0.05  $\mu\text{m}$  alumina suspension (Buehler, EEUU). The samples were etched by a solution consisting on 0.5 g of oxalic acid, 2.5 mL of acetic acid, and 25 mL of absolute ethanol (Sigma-Aldrich, USA).

Field-emission gun scanning electron microscopy (FEG-SEM) (Carl Zeiss AG - EVO<sup>®</sup> 50 Series, Zeiss, Germany) equipped with X-ray energy-dispersive spectrometry (EDS) detector (Oxford Instruments, Aztec Energy, UK) was used for microstructural characterization. ImageJ software (National Institutes of Health, MD) was used to determine the area and the distribution of the secondary phases on transversal and longitudinal sections of the samples.

The composition of the samples was studied by X-ray diffraction (XRD, D8 ADVANCE Twin, Bruker, USA), with Cu K $\alpha$  operating at 40 kV and 100 mA and scanning from 20° to 90°. The scan rate was 2° min<sup>-1</sup>, and the step size was 0.02°.

## 2.3. Electron Backscattered Diffraction (EBSD) analysis

Microstructural evolution of the samples was studied by Electron Backscattered Diffraction (EBSD) technique (C Nano, Oxford Instruments, UK) interfaced with the FEG-SEM. To achieve good statistical data, the scan area selected was 200  $\mu\text{m}$   $\times$  270  $\mu\text{m}$  with 0.15  $\mu\text{m}$  of step size for all the conditions. All the data were processed with CHANNEL 5 software (Oxford Instruments, UK). The grains were defined as a set of minimum 10 points with a mutual misorientation < 10°. Prior to EBSD analysis, the surfaces were prepared by standard mechanical procedures until final polishing with 0.05  $\mu\text{m}$  alumina suspension.

## 2.4. High-speed nanoindentation mapping

Nanoindentations were performed by a KLA iMicro nanoindenter (KLA, USA) using a diamond Berkovich tip with its area function determined against fused silica standard. Each indent performed on complete indentation cycle per second. Matrixes of 100  $\times$  100 indentations were carried out to a maximum constant load of 1 mN with 2  $\mu\text{m}$  spacing between the indents. In all, 10<sup>4</sup> indents were performed to map the processed samples for obtaining reliable correlations at the micrometre length and for subsequent statistical analysis. Results were analyzed by InView software (KLA, USA). Prior to nanoindentation studies, the samples were grinded up to 2500 grit and polished with alumina suspension down to 0.05  $\mu\text{m}$ .

## 2.5. Mechanical characterization

Mechanical properties before and after ECAP process were evaluated by Vickers micro-hardness and tensile tests. Microhardness measurements were performed on the transversal and longitudinal direction of the samples with an indenter load of 100 g and dwelling time of 10 s using a Vickers microhardness tester (Durascan G5, Emctest). According to the obtained results, the E0 and the E2 condition were selected for the following characterization. Tensile dog-bone samples (20 mm gage length, 4 mm diameter, and 8 mm

radius of fillet) were machined along the ECAP direction. Tensile tests were carried out following ASTM E8/E8M [28] with an electromechanical testing frame (MTS Alliance RT/100, MTS system, USA) at room temperature and a displacement rate of 1 mm/min. The tensile tests were replicated using three samples per each condition.

## 2.6. Corrosion characterization

The corrosion behaviour of the samples was studied by potentiodynamic polarization (PDP) tests and static immersion tests at 37  $\pm$  1 °C and pH 7.4  $\pm$  0.1 in Hanks' solution containing 0.4 g/L of KCl, 0.06 g/L of KH<sub>2</sub>PO<sub>4</sub>, 8 g/L of NaCl, 0.045 g/L of Na<sub>2</sub>HPO<sub>4</sub>, 0.35 g/L of NaHCO<sub>3</sub>, and 0.19 g/L of CaCl<sub>2</sub>.

PDP analysis was performed using a PARSTAT 2273 potentiostat (Princeton Applied Research, USA) where a three-electrode set up with a Pt electrode as counter electrode and saturated calomel electrode (SCE) as reference electrode were used. The open circuit potential (OCP) was first measured until its stabilization. The potential window selected for PDP was from -1.4 to -0.6 V potential against the OCP at a scan rate of 0.16 mV/s, according to ASTM G5-14 [29]. The corrosion rate (CR) was calculated from the Tafel extrapolation using PowerSuit software (Princeton Applied Research, USA), following ASTM G102-89 [30].

Static immersion test was performed following ASTM G31-72 [31]. Samples were first weighted and then immersed during 10 days in 20 mL of Hanks' solution at 37  $\pm$  1 °C. The whole solution was renewed every 24 h to avoid a drift in the pH. The redox potential (E) and the pH were monitored with a Hanna HI 5521 multiparameter (Hanna Instruments, Italy). The Pourbaix diagrams of Zn and Ag in Hanks' solution were calculated by HSC 5.1 Software. After The released Zn<sup>2+</sup> and Ag<sup>+</sup> at 1, 3, 7, and 10 days after immersion were analysed by ICP-MS (7800 ICP-MS, Agilent Technologies). For this purpose, aliquots of the solution were collected and filtered with 0.2  $\mu\text{m}$  filter and latter diluted with 1% HNO<sub>3</sub> (v/v). The CR was determined from mass loss measurements for corroded samples cleaned in a solution of 200 g/L CrO<sub>3</sub>(s) at 70  $\pm$  1 °C, according to ISO 8407 [32]. Surface morphology of the samples before and after the removal of the corrosion products were observed by SEM equipped with X-ray energy dispersive spectrometry (EDS) (JSM-7001F, JEOL, Japan).

## 2.7. Bacterial adhesion

*S. aureus* (CCUG 15915, Culture Collection University of Göteborg (CCUG), Göteborg, Sweden) was selected to evaluate the antibacterial properties of the samples. Bacteria in frozen stock were aerobically cultured at 37  $\pm$  1 °C in a brain heart infusion (BHI, Scharlab, Spain) overnight. Bacteria concentration was adjusted to a final optical density of 0.2 at 600 nm, which corresponds to 10<sup>8</sup> colony forming units (CFU) per millilitre.

Two extra conditions were introduced as controls for the adhesion test: Ti and pure Zn discs were prepared following the same metallographic procedure described at section 2.1. Samples were inoculated with 20  $\mu\text{L}$  of bacteria suspension for 3 h. Subsequently, samples were rinsed in phosphate buffer solution (PBS) to remove the non-adhered bacteria.

The LIVE/DEAD<sup>™</sup> BacLight<sup>™</sup> bacterial viability kit (Thermo Fisher, USA) was used to observe the attached alive bacteria (fluorescent green) and dead bacteria (fluorescent red). The staining was prepared by diluting the component SYTO 9 and propidium iodide (1.67 mM) in PBS to a final concentration of 3  $\mu\text{m}$ /mL. For the live/dead staining, adhered bacteria were fixed with 500  $\mu\text{L}$  of 2.5% glutaraldehyde in PBS at 5  $\pm$  1 °C for 30 min and incubated in the staining for 15 min. Afterwards, bacteria were observed by fluorescence microscopy (Nikon E600, Tokyo, Japan). For the quan-



tification of the attached bacteria, samples were introduced in PBS and ultrasonically cleaned for 1 min. The resulting detached bacteria were incubated in agar plates overnight and the number of colony forming units (CFU) were counted.

## 2.8. Statistical analysis

The results of this work were reported as the mean values  $\pm$  standard deviation (SD). Unless previously specified, three replicates ( $n = 3$ ) were done in the experiments. For statistical analysis, a first normality test (Shapiro-Wilk test) was performed to evaluate the normal distribution of the data. Later, an equality of variances test (ANOVA) or a non-parametric test (Kruskal-Wallis test) were performed when data were normally or non-normally distributed, respectively. Minitab Statistical Software (Minitab Inc., USA) was used for the statistical analysis.

## 3. Results

### 3.1. Microstructure characterization

Fig. 1 shows the SEM micrographs of E0, E1, and E2. The microstructure of all the samples was composed by two phases: Zn and  $\text{AgZn}_3$ . According to EDS and XRD results (Fig. 2), and to the Zn-Ag phase diagram [33], the darker area corresponds to the Zn matrix and the brighter area is the secondary  $\text{AgZn}_3$  phase. The microstructure of E0 presented a homogeneous distribution of the  $\text{AgZn}_3$  phase, with a certain alignment to the rolling direction (Fig. 1a,d). Image analysis confirmed similar distribution of the  $\text{AgZn}_3$  phase through the Zn matrix for E1 and E2 samples, with  $\text{AgZn}_3$  particles with areas ranging from 0.05 to  $2.5 \mu\text{m}^2$ , with no observable evidence of fragmentation of the secondary phases.

### 3.2. EBSD analysis

Fig. 3 shows the transversal and longitudinal EBSD inverse pole figure (IPF) maps of the samples, and the data analysis of the grain size is included in Fig. 4. After ECAP, it could be noticed the grain refinement and a more homogeneous grain size distribution from EBSD-IPF maps in both directions. Fig. 3d presents the longitudinal section of E0, showing preferential grain orientation due to the rolling process. However, the oriented and elongated Zn grains of

the alloy became homogenous and non-oriented after ECAP processing (Fig. 3e,f).

Fig. 4 shows larger data dispersion for the grain distribution of E0, which approached a refined log-normal distribution after ECAP. Moreover, the UFG structure was obtained for E1 and E2, reaching grain size values below  $1 \mu\text{m}^2$ . The statistical analysis corroborated significant grain refinement after each ECAP pass.

Fig. 5 shows the IPF of the analysed samples. The weak texture in the transversal direction remained substantially similar after the ECAP process (Fig. 5 a-c). However, it is observed that the ECAP deformation caused noticeable changes in the longitudinal direction (Fig. 5 d-f). From the IPF of the longitudinal section of the E0 condition, it is evident that the majority of grains were preferentially oriented to [0001] pole and scattered to the other directions with the ECAP cycles, developing a more random texture.

### 3.3. High-speed nanoindentation mapping

The nanohardness and the elastic modulus maps obtained after high-speed nanoindentation tests are shown in Fig. 6 and Fig. 7, respectively, and quantified in Table 1. Mechanically different areas could be perfectly distinguished from the transversal section maps of E0 (Fig. 6a, Fig. 7a). The hardness became more isotropic on the transversal section after ECAP (Fig. 6 b,c), together with a significantly lower average nanohardness values indicating the softening of the material (Table 1). Regarding this, a similar homogeneity trend could be observed from elastic modulus maps of E1 and E2 transversal section analysis (Fig. 7 b,c). Even though the qualitative tendency is clear, the nanohardness and elastic modulus values provided in Table 1 were calculated as an average from the maps without considering the presence of two phases. Therefore, no quantitative comparison among conditions should be extracted from the reported values, which might be affected by the local distribution of the  $\text{AgZn}_3$  phase in the tested area.

### 3.4. Mechanical characterization

The evaluation of the mechanical behaviour was performed by means of microhardness measurements and of tensile tests. The hardness values and tensile curves collected are summarized in Fig. 8. The E0 microhardness showed a clear drop for both directions after the second ECAP cycle (Fig. 8 a). For this reason, the subsequent tensile characterization was focused on the E2 condition

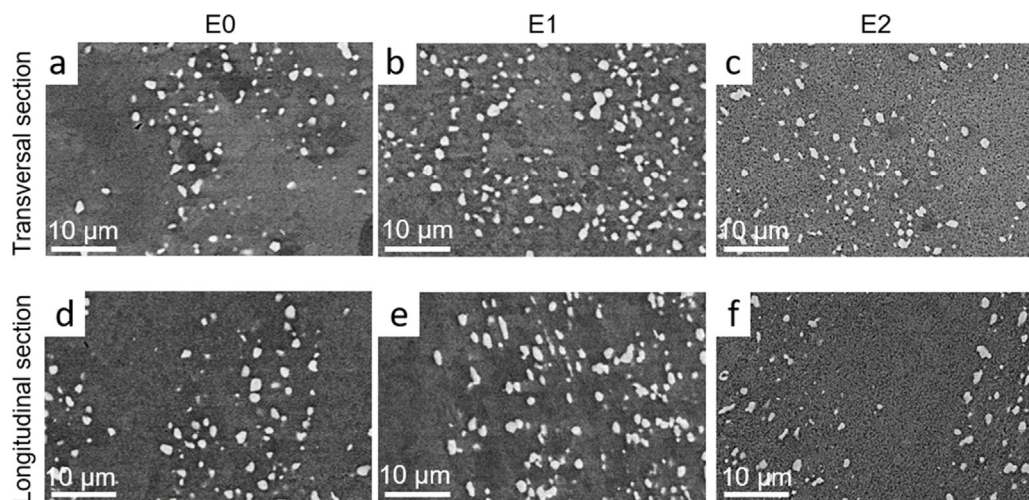
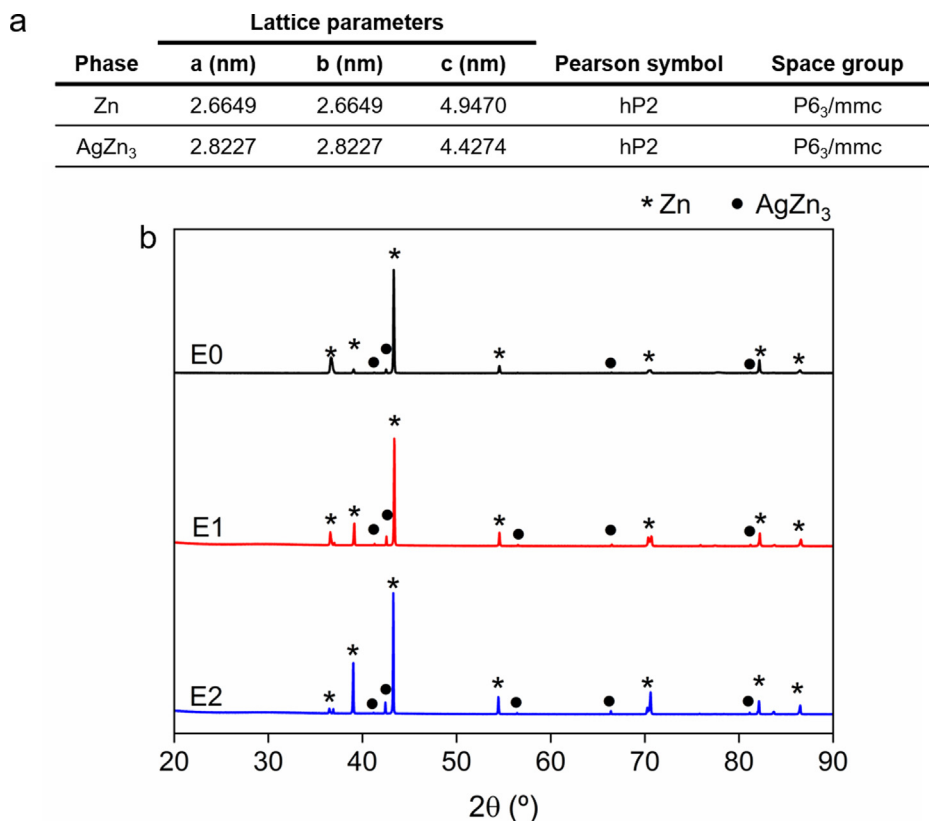
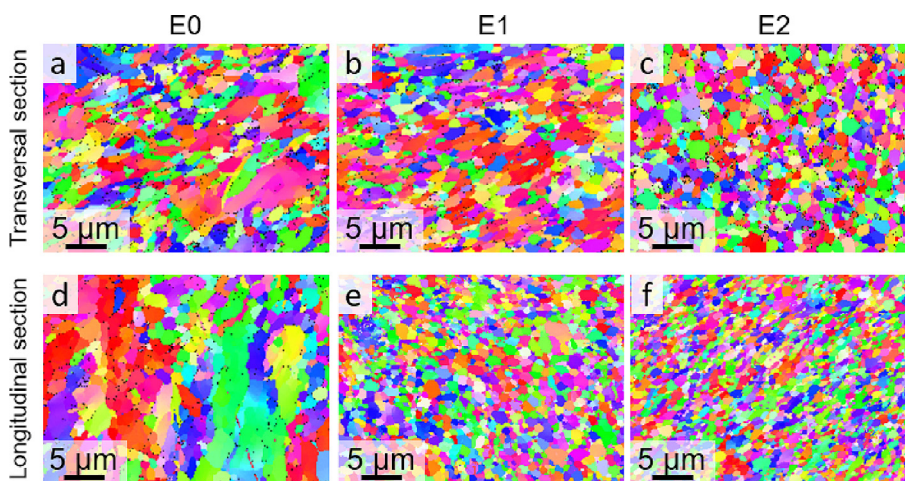


Fig. 1. Microstructure of the transversal sections (top) and longitudinal sections (bottom) of E0 (a, d), E1 (b, e), and E2 (c, f). The darker area corresponds to the Zn matrix and the brighter area is the  $\text{AgZn}_3$  phase.



**Fig. 2.** XRD results: (a) Crystallographic data of Zn and AgZn<sub>3</sub> phases. (b) XRD spectra of E0, E1, and E2 samples.



**Fig. 3.** EBSD-IPF map of the transversal section (top) and longitudinal section (bottom) of ZnAg at the different stages: as-received (a, d), after first ECAP cycle (b, e), and after second ECAP cycle (c, f).

only. The tensile tests (Fig. 8 b) showed an important decrease in the ultimate tensile strength (UTS) and yield strength (YS) after two ECAP cycles. Both tested materials featured a very limited work hardening ability in the plastic regime but extensive ductility, reaching values of fracture elongation ( $A\%$ ) above 200 % for the E2 samples. Fig. 8 includes representative fractographs of the samples after the tensile test. The fracture morphology of the E0 mainly showed dimples with diameter of in the range 2–20  $\mu\text{m}$  (Fig. 8 c) whereas the dimple size decreased below 2  $\mu\text{m}$  for the E2 sample (Fig. 8 d), in accordance to the observed microstructure structure refinement.

### 3.5. Corrosion characterization

The corrosion parameters calculated from PDP and immersion tests in Hanks' solution are listed in Table 2. No significant differences were observed between E0 and E2 samples for any parameter (Table 2). The values obtained are in accordance with previous corrosion studies on Zn-Ag alloys [34].

Although the corrosion parameters presented no statistical differences, the ion release of the samples differed. As shown in Fig. 9a, the release of  $\text{Zn}^{2+}$  was higher for E2 in comparison with E0, with a total final concentration of  $20.66 \pm 0.24 \mu\text{g/dL}$  and 13.



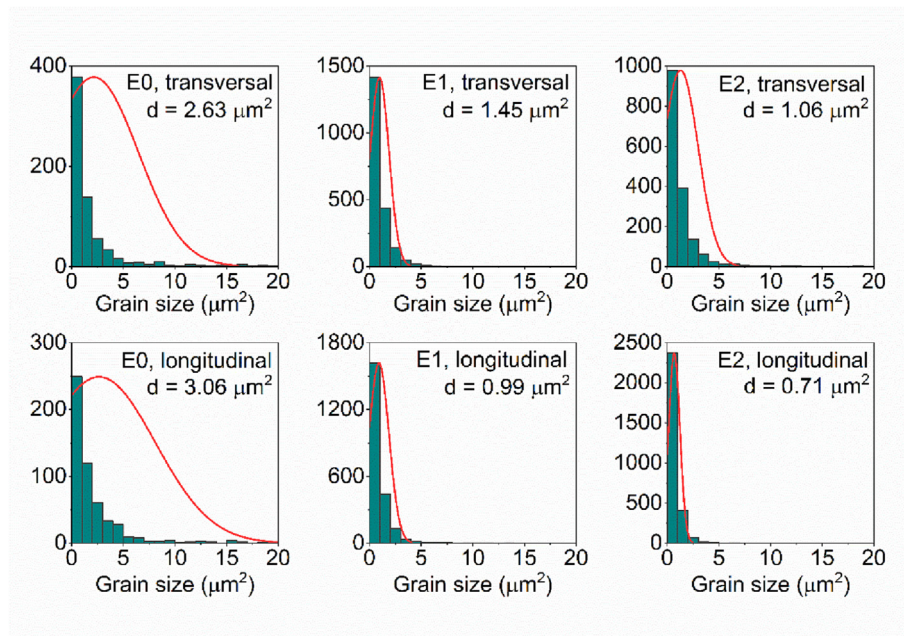


**Fig. 4.** Bar charts based on binned grain size populations the as-received and ECAP samples at the transversal and longitudinal sections; and the calculated grain size values using CHANNEL 5 software.

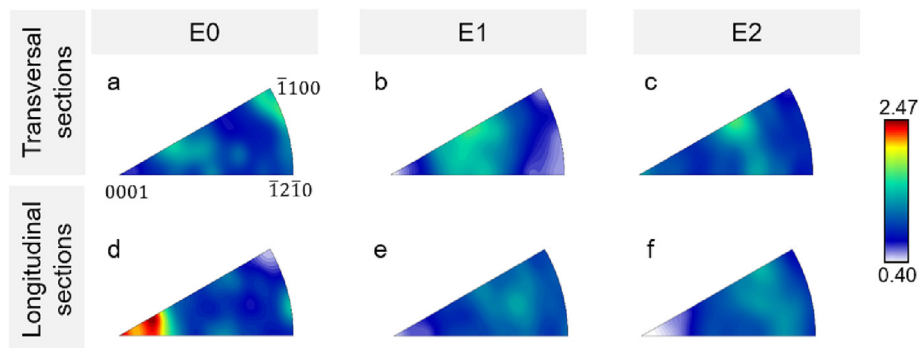


**Fig. 5.** IPF images of the transversal and longitudinal sections of E0, E1, and E2 samples.

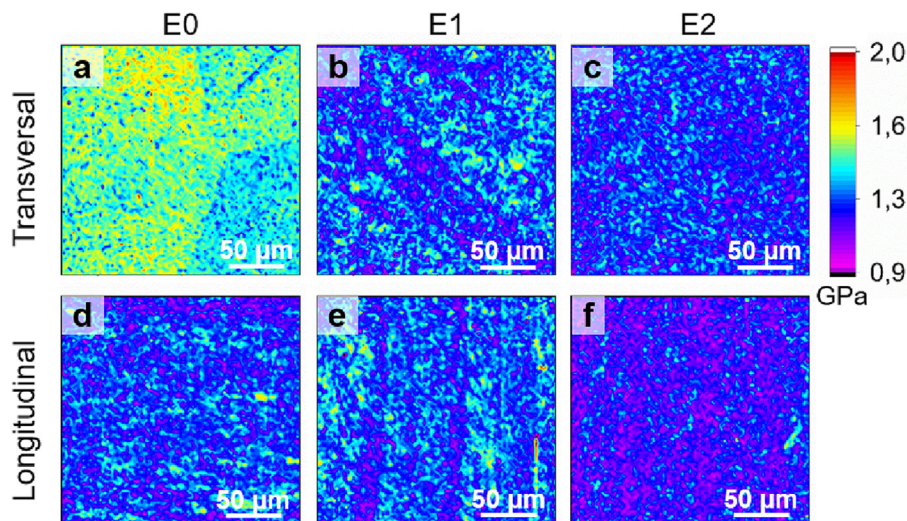


**Fig. 6.** Hardness nanoindentation maps of E0 (a, d), E1 (b, e), and E2 (c, f) at the transversal (top) and longitudinal (bottom) sections. Scale bar: 50  $\mu\text{m}$ .

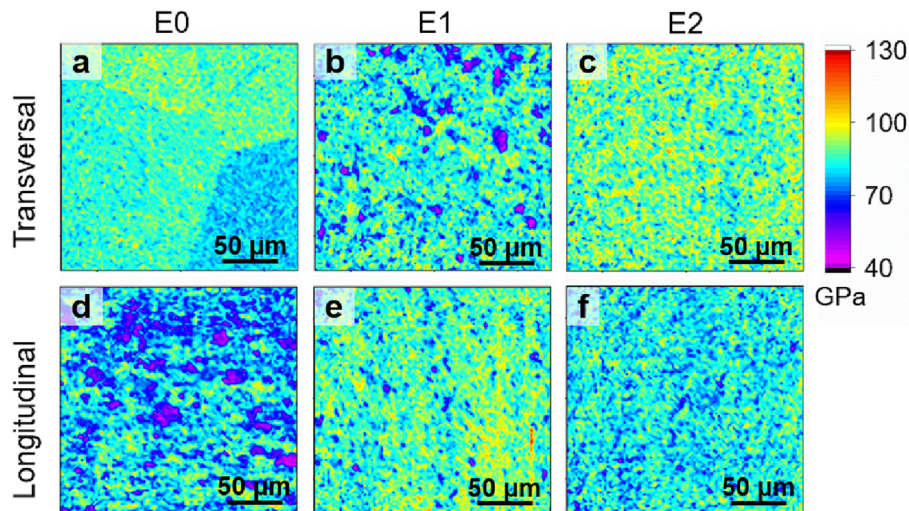


Fig. 7. Elastic modulus nanoindentation maps of E0 (a, d), E1 (b, e), and E2 (c, f) at the transversal (top) and longitudinal (bottom) sections. Scale bar: 50  $\mu\text{m}$ .

Table 1

Elastic modulus (E) and nanohardness (H) parameters calculated from nanoindentation maps of the transversal and longitudinal section of E0, E1, and E2.

Direction	E0		E1		E2	
	Transversal	Longitudinal	Transversal	Longitudinal	Transversal	Longitudinal
H (GPa)	$1.47 \pm 0.13$	$1.25 \pm 0.13$	$1.26 \pm 0.14$	$1.28 \pm 0.14$	$1.24 \pm 0.13$	$1.18 \pm 0.12$
E (GPa)	$84.9 \pm 6.7$	$77.3 \pm 12.0$	$82.1 \pm 10.8$	$86.2 \pm 9.8$	$88.2 \pm 9.8$	$81.8 \pm 9.5$

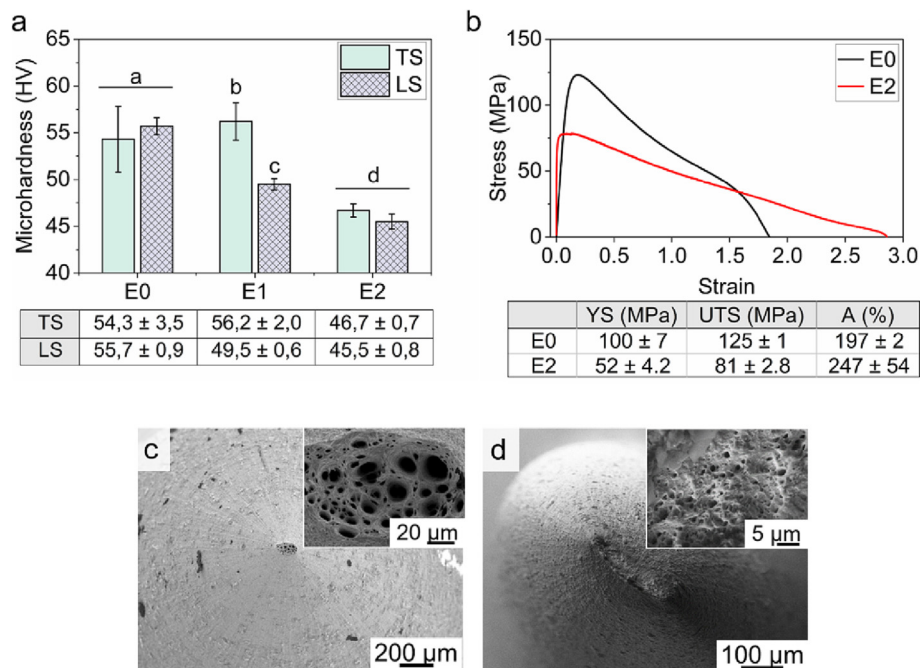
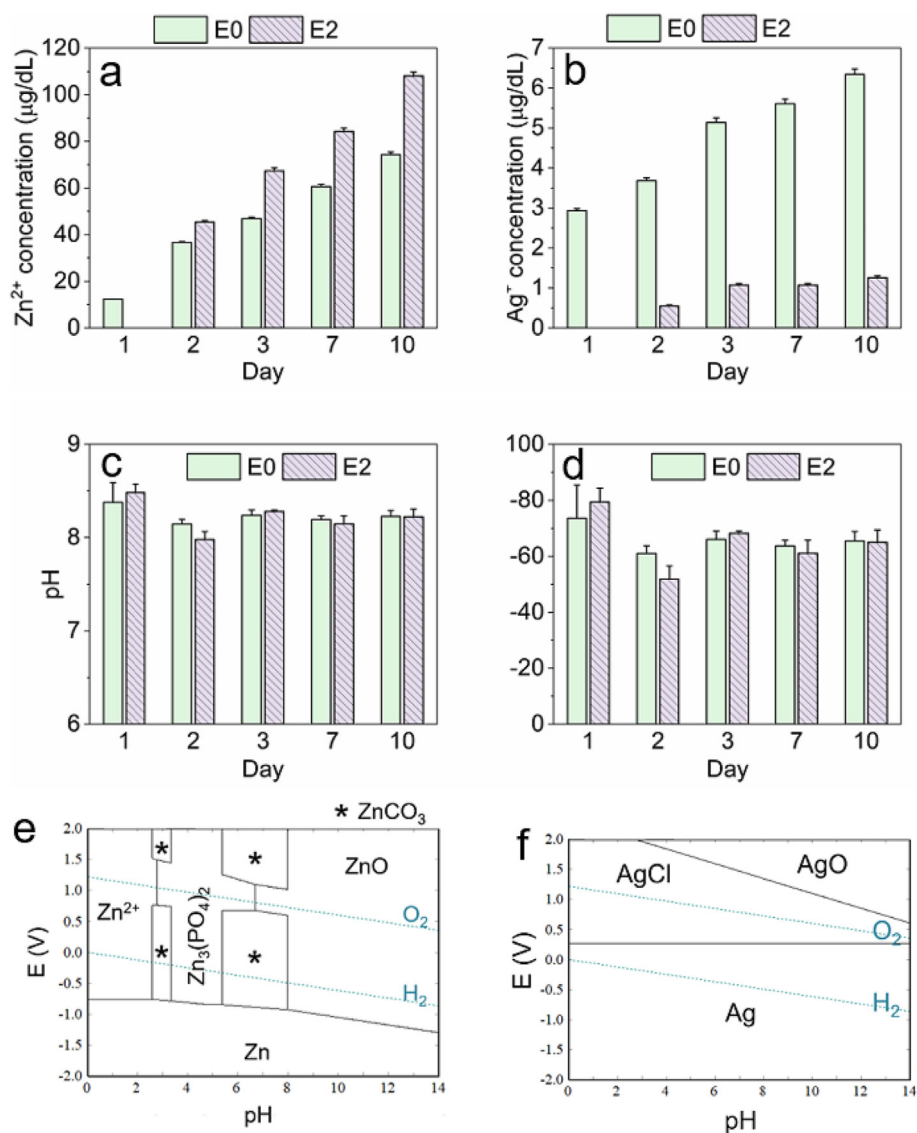


Fig. 8. (a) Vickers micro-hardness results of E0, E1, and E2 samples. <sup>a,b,c,d</sup> symbols join groups with non-statistically significant differences. (b) Tensile curves and calculated tensile properties of the E0 and E2 samples. SEM fractographic images of (c) E0, and (d) E2 samples.

Table 2

Corrosion parameters obtained from PDP and static immersion test in Hanks' solution: corrosion potential (E), current density (i), CR (PDP), and CR (mass loss).

	E (V)	i ( $\mu\text{A}/\text{cm}^2$ )	CR, PDP (mm/yr)	CR, mass loss (mm/yr)
E0	$-1.176 \pm 0.018$	$2.26 \pm 0.13$	$0.034 \pm 0.002$	$0.099 \pm 0.032$
E2	$-1.193 \pm 0.008$	$1.98 \pm 0.43$	$0.029 \pm 0.006$	$0.090 \pm 0.046$



**Fig. 9.** Accumulative (a) Zn<sup>2+</sup> and (b) Ag<sup>+</sup> ion release of the samples measured by ICP-MS after 1, 2, 3, 7, and 10 days of immersion. Evolution of (c) pH, and (d) E with the immersion time. Pourbaix diagrams of (e) Zn, and (f) Ag in Hanks' solution at tested conditions obtained by HSC 5.1 Software.

**Table 3**

ICP-MS results of released Zn<sup>2+</sup> and Ag<sup>+</sup> at days 1, 2, 3, 7, and 10 of immersion in Hanks' solution at 37 ± 1 °C. Limit of detection (LOD): Zn<sup>2+</sup> = 0.01 μg/dL; Ag<sup>+</sup> = 0.001 μg/dL.

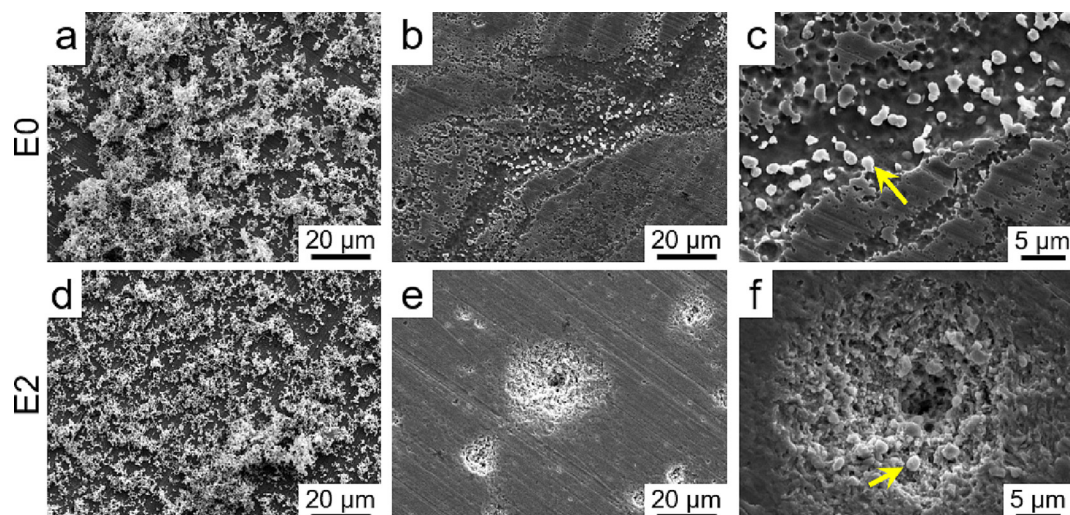
Day	E0		E2	
	Zn <sup>2+</sup> (μg/dL)	Ag <sup>+</sup> (μg/dL)	Zn <sup>2+</sup> (μg/dL)	Ag <sup>+</sup> (μg/dL)
1	12.26 ± 0.03 (81%)	2.93 ± 0.05 (19 %)	<LOD	<LOD
2	24.37 ± 0.30 (97 %)	0.75 ± 0.02 (3 %)	45.46 ± 0.58 (99 %)	0.55 ± 0.02 (1 %)
3	10.22 ± 0.40 (88 %)	1.46 ± 0.04 (12 %)	21.88 ± 0.74 (98 %)	0.52 ± 0.01 (2 %)
7	13.81 ± 0.20 (97 %)	0.47 ± 0.01 (3 %)	16.97 ± 0.08 (100 %)	<LOD
10	13.66 ± 0.16 (95 %)	0.74 ± 0.02 (5 %)	23.78 ± 0.24 (99 %)	0.19 ± 0.01 (1 %)

69 ± 0.21 μg/dL, respectively. On the other hand, the Ag<sup>+</sup> release presented the opposite relation, with lower total concentration for E2 (0.11 ± 0.01 μg/dL) than for E0 (0.92 ± 0.02 μg/dL) (Fig. 9b). Table 3 shows the Zn<sup>2+</sup> and Ag<sup>+</sup> concentrations measured by ICP-MS on days 1, 2, 3, 7, and 10 of immersion and their relation in %. Fig. 9c,d show the pH and the E evolution through the immersion test in Hanks' solution, respectively. As expected, the pH increased respect to the initial value of 7.4, confirming the release of corrosion products from the alloys. The obtained values of E were between -40 and -80 mV. The calculated Pourbaix diagrams of Zn and Ag in Hanks' are depicted in Fig. 9 e,f. Applying the

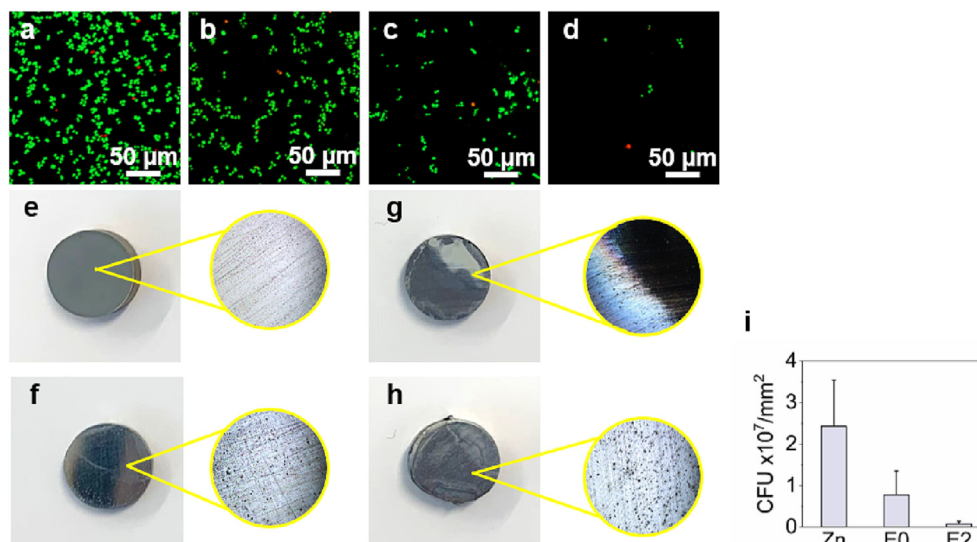
obtained values of pH and E in the Pourbaix diagrams, the most stable Zn solid phases are ZnCO<sub>3</sub>(s) and ZnO (s) while the most stable Ag solid phases are Ag(s), and AgCl (s).

Fig. 10 shows the SEM images of the surfaces of E0 and E2 with the corrosion products after the immersion test. The corrosion layer formed onto both studied surfaces was homogeneous, as it can be seen in Fig. 10 a,d. The elemental analysis performed by EDS detected Zn, Ca, C, O, P, and Cl, as a result of the precipitation of calcium phosphate minerals, and Zn-carbonates, phosphates and oxides and Ag-chloride as predicted by the Pourbaix diagrams [33,35]. Besides, EDS mapping indicated the presence of Zn and





**Fig. 10.** SEM images of the E0 and E2 sample surfaces after 10 days of immersion in Hanks' solution: before (a, d) and after (b-c, e-f) the removal of the corrosion products. Yellow arrows indicate the non-degraded  $\text{AgZn}_3$  phase. (For interpretation of the references to colour in this figure legend, the reader is referred to the web version of this article.)



**Fig. 11.** Bacterial adhesion tests of the studied surfaces cultured with *S. Aureus* after 3 h of incubation. Live-dead staining of *S. Aureus* incubated onto (a) Ti, (b) Zn, (c) E0, and (d) E2. Images of the surfaces after the adhesion test and subsequent cleaning: (e) Ti, (f) Zn, (g) E0, and (h) E2. (i) Quantification of attached bacteria to the surfaces. Ti is not included since it exceeded the maximum CFU for quantification.

Ag located at the underlying metallic surface. SEM images of the corroded surfaces after the removal of the corrosion layer showed similar corrosion features for both E0 (Fig. 10 b,c) and E2 (Fig. 10 e, f), with the most stable  $\text{AgZn}_3$  phase surrounded by the anodic degradation of the Zn matrix.

### 3.6. Bacterial response

The bacterial response was evaluated after 3 h of culture with *S. Aureus* on inert c.p. Ti and Zn, as controls, and on the investigated E0, and E2 samples. Fig. 11 a-d shows the confocal images obtained after the live-dead assay. Ti surface was totally covered by bacteria (Fig. 11 a), exceeding the maximum limit for CFU quantification at the tested conditions. On the other hand, the reduced bacteria attachment to Zn-based surfaces (Fig. 11 b-d), indicated a noticeable antibacterial activity compared with Ti. In addition, the antibacterial performance of E0 significantly reduced the bacterial attachment, from  $(2.4 \pm 1.1) \times 10^7$  CFU/ $\text{mm}^2$  of the Zn surface (Fig. 11 b), to

$(7.8 \pm 5.8) \times 10^6$  CFU/ $\text{mm}^2$  of the E0 alloy. Surprisingly, the ECAP deformation accentuated the antibacterial effect (Fig. 11 d), with a noticeable reduction in CFU, down to  $(7.6 \pm 5.9) \times 10^5$  CFU/ $\text{mm}^2$ .

Fig. 11 e-h includes the general image of the metallic surfaces after the bacterial adhesion test, and subsequent cleaning with ethanol and ultrasounds. The surface of Ti remained intact, according to its inert nature (Fig. 11 e). In contrast, degradation signs could be observed in the Zn-based samples (Fig. 11 f-h). Pure Zn and E2 samples showed distributed degradation pits, whereas the E0 presented a heterogeneously degraded surface with a pronounced degradation compared to the studied series.

## 4. Discussion

Biodegradable metals emerged to overcome the drawbacks of conventional implants, including inflammation processes, long-term consequences, or second surgeries for their removal [36,37]. Among them, Zn stands out due to its biocompatibility and degra-

dation rate [38]. However, its insufficient mechanical properties force to alloy Zn with other elements, strengthening the material *via* solid solution, grain refining and precipitation hardening, but inevitably modifying the degradation behaviour and affecting the biological behaviour of the alloys [39]. Thus, extensive research is focused on modifying the secondary phases' distribution to obtain a homogeneous microstructure [40,41]. Here, no relevant changes were noticed in the AgZn<sub>3</sub> area or distribution. Xu et al. [42] performed an extensive analysis of Zn-based alloys after ECAP, in which they reported the breaking and the formation of secondary phases with ECAP passes. Here, a possible combination of both mechanisms would lead to no observable changes in the AgZn<sub>3</sub> distribution. Nevertheless, further analysis should be done to verify this hypothesis. In this regard, the mechanical isotropy of a material has direct effects on its mechanical performance, enhancing the safety of the implants and increasing the implantation tolerance [43–45]. Several studies have been performed to control anisotropy or to fabricate isotropic structures [44,46]. In this work, two ECAP cycles have been successfully applied to a Zn-2Ag alloy in order to obtain a homogeneous UFG structure. The excellent starting formability of the material allowed two ECAP passes to be performed at room temperature, avoiding any failure [47], hence providing an additional degree of freedom for the control of the final microstructure. The as-received Zn-2Ag alloy developed UFG microstructure with randomly distributed grain orientation after the ECAP process. Mechanically different regions above 100 µm<sup>2</sup> in the E0 surface were noticed at high-speed nanoindentation mapping (Fig. 6 and Fig. 7), which might be attributed to larger primary Zn grains previously observed in polycrystalline Zn [48]. It is assumed that both nanohardness and elastic modulus are dependent on grain orientation [49,50]. Homogeneous nanohardness (Fig. 6) and elastic modulus (Fig. 7) were reported for both E1 and E2 samples. The direct influence of the secondary phases in the final mechanical performance in binary Zn-based alloys has been previously reported [39]. Here, the average results of both elastic modulus and hardness is calculated without considering the presence of two phases, since the equipment was not sensible enough to distinguish between the Zn matrix and the small areas occupied by the AgZn<sub>3</sub> phase. The mechanical properties of hexagonal-closed pack (hcp) alloys have been reported to be closely related to the texture [51]. However, despite the homogeneous texture, Vickers-hardness measurements evidenced the isotropic response only for E2 (Fig. 8 a), suggesting that the grain size and crystal orientation may be playing a fundamental role in the mechanical behaviour of the samples. The differences in nanohardness and Vickers might be related to an overestimation of nanohardness values due to indentation size effects because of the small indentation depths used. As previously reported by Bednarczyk et al. [14], ECAP process is almost ineffective in strengthening hcp materials but it does induce a dramatic change in grain size and crystal texture. Indeed, after as-received cold-rolled rods a sharp texture is observed. The low crystal symmetry in hcp structures results in the activation of only one slip system per grain, diminishing the possibility of dislocations slip within the grains and thus, increasing material strength [52]. After ECAP, the crystal refinement and orientation redistribution results in lower texture, hence easier slip of dislocations which better accommodates the macroscopic deformation resulting in lower YS, UTS, and exceptional fracture elongation (Fig. 8) [53,54]. Moreover, another study by Bednarczyk et al. [55] reported an inverse Hall-Petch phenomenon in Zn-0.8Ag after severe plastic deformation. They corroborated that after extensive grain refinement, the slope of Hall-Petch could become negative and lead to a softening of the material, where grain boundary sliding (GBS) mechanisms would predominate. Nonetheless, the obtained YS and UTS around 50 and 80 MPa, respectively, are still superior to those of actual bioresorbable polymeric sutures (UTS: 40 – 60 MPa [56,57]).

This superior mechanical strength would avoid complex multi-braid structures, in which the risk of bacterial infection is higher. Moreover, the obtained high elongation to fracture is supposed to provide good formability, good handling and knot security [58].

It has been widely reported that the refinement of the microstructure improves corrosion protection and reduces localized corrosion [17,59]. This is due to the refinement and homogeneous distribution of the secondary phases, which minimizes its cathodic capacity and hence the possible galvanic pairs lose their effectiveness [16,17]. On the other side, grain refinement could accelerate corrosion by the increased Gibb's free energy related to grain boundaries surface, whose concentration is higher in UFG structures [60]. These two effects might also compensate each other, leaving the corrosion rate of the SPD alloy substantially unchanged. In our studies, similar corrosion parameters were found for E0 and E2 samples in Hanks' solution (Table 2), but the ICP-MS measurements provided some differences regarding the ionic release of metallic species (Table 3). The total release of Zn<sup>2+</sup> detected for both samples is in the physiological range (2–15 µM) [61], with a final total concentration of 3.1 µM and 2.1 µM for E2 and E0, respectively. Interestingly, the Ag<sup>+</sup> release seemed to be hindered after the ECAP process. The E0 exhibited a first burst release on day 1, and fluctuating Ag<sup>+</sup> concentrations ranging from 3 to 12 % of the total measured ion release the following days. (Table 3). In contrast, E2 presented a more homogeneous release of 1–2 % of Ag<sup>+</sup> through the experiment, in which the percentage of released Zn<sup>2+</sup> in the E2 increased up to 98–99 %. This sustained release might be related to a modification in the area or distribution of the AgZn<sub>3</sub> phase after ECAP, even if any change was observable in SEM analysis (Fig. 1), as well as a more homogeneous Ag distribution into the Zn matrix. However, further characterization should be performed to confirm these hypotheses. The excessive administration of silver may have genotoxic effects, but further studies would be needed to assess its carcinogenic potential [62,63]. Recently, Guillory et al. [64] observed a positive *in vivo* performance of Zn-based wires with 4 wt% of Ag implanted into female Sprague Dawley rats for 6 months. Thus, the amount of delivered Ag<sup>+</sup> of E0 series should not have a cytotoxic effect. Finally, the degradation time for actual biomaterials used for wound closure are 4–6 weeks, for PLA/PGA 75/25 and PGA, or more than 1.5–5 years, for PLA [3]. Assuming a constant corrosion rate of 0.090 mm/year (Table 2), a typical USP 5–0 suture (Ø 100 µm) [65] would degrade at an intermediate time of 6 months after implantation.

Bacterial infection is a worldwide theme of concern due to the medical resistance developed by bacterial strains such as *S. aureus*, which is the most common strain present in skin, soft tissue, bone, joints, and device-associated infections [24]. Recently, the investigation focused on new antibacterial approaches for biomaterials has attracted global interest. The use of metallic ions such as copper or silver as antibacterial agents have been investigated for different biomaterials [25]. Ti is a common biomaterial used for wound suture applications; however, Ti requires to be treated to avoid possible bacterial infections [26]. A possible strategy includes the introduction of ZnO onto Ti-based materials due to its well-known antibacterial effect properties [66–69]. Therefore, the reduced number of bacteria attached to Zn-based surfaces (Fig. 11) may be related with the presence of a ZnO in its natural passivation layer. As expected, the presence of Ag in the Zn-Ag alloys reduced the bacterial attachment. The minimum inhibitory concentration (MIC) reported of colloidal silver is 1.39 mg/dL [69], and the reported MIC for silver nanoparticles 0.625 mg/dL [70]. Both values are much superior to the total Ag<sup>+</sup> detected at the immersion test, thus, the decreased bacterial adhesion of Zn-Ag alloys was not related to Ag<sup>+</sup> diffusion mechanisms, but to the Ag presence onto the metallic surfaces and its antibacterial effect

by contact. Surprisingly, the antibacterial activity was considerably enhanced after ECAP processing. Previous reports have shown lower bacterial adhesion to polymeric and thus, softer surfaces [71], but the opposite trend in polymeric materials has also been published [72]. Nonetheless, most of the studies are referring to polymeric surface that intrinsically offer mesh-like structures in which other factors as porosity may be affecting bacterial adhesion [71]. Thus, the relation between the surface hardness and the bacterial adhesion would require further investigation. Regarding this, the supposition of a better Ag distribution after ECAP would contribute to the greater antibacterial effect observed in the E2 sample.

Another important observation was the different aspect of the degraded E0 and E2 sample surfaces after the bacterial adhesion test (Fig. 11), in contrast to the similar corroded surface after corrosion tests in Hanks' solution. In previous studies, the changing degradation behaviour of Zn surfaces depending on the immersion media has been studied [73,74]. Furthermore, an extensive characterization of Zn and Zn-4Ag in different corrosive media has been performed by Sikora-Janinska et al. [75], in which the presence of organic species was reported to form a passivation layer and protect the surfaces from further corrosion. Biodegradable implants may avoid bacterial infection by providing a non-stable surface for bacterial adhesion [76]. However, the accumulation of bacteria onto the degraded and rougher surfaces of Zn-based alloys has been previously reported [39]. In connection with our bacterial test, the more degraded surface of E0 may limit the antibacterial effect, whereas the uniform surface degradation of E2 provided a smoother surface to which bacteria hardly attached, contributing to the enhancement of the antibacterial activity.

## 5. Conclusions

In this work, Zn-2Ag was successfully subjected to ECAP at room temperature. The microstructure of the samples consisted of a Zn matrix and a secondary  $\text{AgZn}_3$  phase. EBSD results confirmed the generation of UFG structures after ECAP with randomly distributed texture and similar size and distribution of second phases for E1 and E2 samples. Nanoindentation maps suggested isotropic mechanical properties of the ECAP-processed samples. However, Vickers measurements only confirmed the isotropy for E2, demonstrating the influence of the grain refinement on the nano- and micro-mechanical performance of the material. Lower UTS and YS with higher elongation have been reported after ECAP, in accordance with previous studies on hcp materials. Similar corrosion rates were observed for E0 and E2 in Hanks' solution, with a released concentration of  $\text{Zn}^{2+}$  among the physiological range of 2–15 mM. The more homogeneous  $\text{Ag}^+$  release of E2 sample was attributed to the better Ag distribution along the Zn matrix after ECAP process. The released  $\text{Ag}^+$  was below the MIC for *S. Aureus*, and hence the observed antibacterial effect was attributed to the bacterial contact with the Ag-containing surfaces. Moreover, the better Ag distribution in E2 and its uniformly degraded surface after the bacterial adhesion test would contribute to the excellent antibacterial performance of the sample. In summary, the ECAP process provided mechanical isotropy, good formability, and exceptional antibacterial activity to biodegradable Zn-2Ag, being a potential processing route candidate for the manufacturing of wires for wound closure applications.

## CRediT authorship contribution statement

**García-Mintegui Claudia:** Investigation, Methodology, Writing – original draft. **S. Goncharov Ivan:** Investigation, Methodology. **Ortiz-Membrado Laia:** Investigation. **Jiménez-Piqué Emilio:**

Investigation. **Ginebra Maria-Pau:** Supervision, Funding acquisition. **Vedani Maurizio:** Writing – review & editing, Supervision, Validation, Methodology, Funding acquisition. **Cortina José Luís:** Writing – review & editing, Supervision, Validation, Funding acquisition. **Pegueroles Marta:** Writing – review & editing, Supervision, Formal analysis, Methodology, Funding acquisition.

## Data availability

Data will be made available on request.

## Declaration of Competing Interest

The authors declare that they have no known competing financial interests or personal relationships that could have appeared to influence the work reported in this paper.

## Acknowledgements

Financial support was received from Spanish Government, MCIN/ AEI / 10.13039/501100011033 / FEDER, UE, (PID2021-125150OB-I00) and the Agency for Administration of University and Research Grants of the Government of Catalonia (2021 SGR 01368, 2017SGR-312). Support for the research of M-P.G. was received through the prize “ICREA Academia” for excellence in research, funded by the Generalitat de Catalunya.

## References

- [1] J.J.D. Venezuela, S. Johnston, M.S. Dargusch, The Prospects for Biodegradable Zinc in Wound Closure Applications, *Adv Healthc Mater.* 8 (2019) 1–15, <https://doi.org/10.1002/adhm.201900408>.
- [2] C. Li, C. Guo, V. Fitzpatrick, A. Ibrahim, M.J. Zwierstra, P. Hanna, A. Lechtig, A. Nazarian, S.J. Lin, D.L. Kaplan, Design of biodegradable, implantable devices towards clinical translation, *Nat Rev Mater.* 5 (2020) 61–81, <https://doi.org/10.1038/s41578-019-0150-z>.
- [3] P. Gentile, V. Chiono, I. Carmagnola, P. v. Hatton, An overview of poly(lactic-co-glycolic) Acid (PLGA)-based biomaterials for bone tissue engineering, *Int J Mol Sci.* 15 (2014) 3640–3659, <https://doi.org/10.3390/ijms15033640>.
- [4] A.L. Tajirian, D.J. Goldberg, A review of sutures and other skin closure materials, *Journal of Cosmetic and Laser Therapy.* 12 (2010) 296–302, <https://doi.org/10.3109/14764172.2010.538413>.
- [5] J.M. Seitz, D. Utermöhlen, E. Wulf, C. Klose, F.W. Bach, The manufacture of resorbable suture material from magnesium - Drawing and stranding of thin wires, *Adv Eng Mater.* 13 (2011) 1087–1095, <https://doi.org/10.1002/adem.201100152>.
- [6] J. Venezuela, M.S. Dargusch, The influence of alloying and fabrication techniques on the mechanical properties, biodegradability and biocompatibility of zinc: A comprehensive review, *Acta Biomater.* 87 (2019) 1–40, <https://doi.org/10.1016/j.actbio.2019.01.035>.
- [7] D. Vojtěch, J. Kubásek, J. Šerák, P. Novák, Mechanical and corrosion properties of newly developed biodegradable Zn-based alloys for bone fixation, *Acta Biomater.* 7 (2011) 3515–3522, <https://doi.org/10.1016/j.actbio.2011.05.008>.
- [8] H. Yang, B. Jia, Z. Zhang, X. Qu, G. Li, W. Lin, D. Zhu, K. Dai, Y. Zheng, Alloying design of biodegradable zinc as promising bone implants for load-bearing applications, *Nat Commun.* 11 (2020), <https://doi.org/10.1038/s41467-019-14153-7>.
- [9] Z.Z. Shi, X.X. Gao, H.J. Zhang, X.F. Liu, H.Y. Li, C. Zhou, Y.X. Yin, L.N. Wang, Design biodegradable Zn alloys: Second phases and their significant influences on alloy properties, *Bioact Mater.* 5 (2020) 210–218, <https://doi.org/10.1016/j.bioactmat.2020.02.010>.
- [10] H. Kabir, K. Munir, C. Wen, Y. Li, Recent research and progress of biodegradable zinc alloys and composites for biomedical applications: Biomechanical and biocorrosion perspectives, *Bioact Mater.* 6 (2021) 836–879, <https://doi.org/10.1016/j.bioactmat.2020.09.013>.
- [11] N. Yang, J. Venezuela, S. Almathami, M. Dargusch, Zinc-nutrient element based alloys for absorbable wound closure devices fabrication: Current status, challenges, and future prospects, *Biomaterials.* 280 (2022), <https://doi.org/10.1016/j.biomaterials.2021.121301>.
- [12] H. Guo, R.H. Cao, Y.F. Zheng, J. Bai, F. Xue, C.L. Chu, Diameter-dependent in vitro performance of biodegradable pure zinc wires for suture application, *J Mater Sci Technol.* 35 (2019) 1662–1670, <https://doi.org/10.1016/j.jmst.2019.03.006>.
- [13] H. Liu, H. Huang, Y. Zhang, Y. Xu, C. Wang, J. Sun, J. Jiang, A. Ma, F. Xue, J. Bai, Evolution of Mg–Zn second phases during ECAP at different processing temperatures and its impact on mechanical properties of Zn-1.6Mg (wt.%)



- alloys, *J. Alloys Compd.* 811 (2019), <https://doi.org/10.1016/j.jallcom.2019.151987>.
- [14] W. Bednarczyk, M. Wątroba, J. Kawałko, P. Bała, Can zinc alloys be strengthened by grain refinement? A critical evaluation of the processing of low-alloyed binary zinc alloys using ECAP, *Materials Science and Engineering A* 748 (2019) 357–366, <https://doi.org/10.1016/j.msea.2019.01.117>.
- [15] D.N. Awang Sh'ri, Z.S. Zahari, A. Yamamoto, Effect of ecap die angle on mechanical properties and biocompatibility of ss316L, *Metals (Basel)* 11 (2021), <https://doi.org/10.3390/met11101513>.
- [16] J.X. Chen, X.Y. Zhu, L.L. Tan, K. Yang, X.P. Su, Effects of ECAP Extrusion on the Microstructure, Mechanical Properties and Biodegradability of Mg–2Zn–xGd–0.5Zr Alloys, *Acta Metallurgica Sinica (English Letters)* 34 (2021) 205–216, <https://doi.org/10.1007/s40195-020-01136-7>.
- [17] S. v. Dobatkin, E.A. Lukyanova, N.S. Martynenko, N.Y. Anisimova, M. v. Kiselevskiy, M. v. Gorshenkov, N.Y. Yurchenko, G.I. Raab, V.S. Yusupov, N. Birbilis, G.A. Salishchev, Y.Z. Estrin, Strength, corrosion resistance, and biocompatibility of ultrafine-grained Mg alloys after different modes of severe plastic deformation, in: *IOP Conf Ser Mater Sci Eng*, Institute of Physics Publishing, 2017. 10.1088/1757-899X/194/1/012004.
- [18] X. Zhuo, Y. Wu, J. Ju, H. Liu, J. Jiang, Z. Hu, J. Bai, F. Xue, Recent progress of novel biodegradable zinc alloys: from the perspective of strengthening and toughening, *Journal of Materials Research and Technology*. 17 (2022) 244–269, <https://doi.org/10.1016/j.jmrt.2022.01.004>.
- [19] W. Bednarczyk, J. Kawałko, M. Wątroba, P. Bała, Achieving room temperature superplasticity in the Zn–0.5Cu alloy processed via equal channel angular pressing, *Materials Science and Engineering A*. 723 (2018) 126–133, <https://doi.org/10.1016/j.msea.2018.03.052>.
- [20] F. Gottrup, A. Melling, D.A. Hollander, An overview of surgical site infections: aetiology, incidence and risk factors; An overview of surgical site infections: aetiology, incidence and risk factors, n.d.
- [21] J.W. Alexander, J.S. Solomkin, M.J. Edwards, Updated recommendations for control of surgical site infections, *Ann Surg.* 253 (2011) 1082–1093, <https://doi.org/10.1097/SLA.0b013e31821175f8>.
- [22] I. Ahmed, A.J. Boulton, S. Rizvi, W. Carlos, E. Dickenson, N.A. Smith, M. Reed, The use of triclosan-coated sutures to prevent surgical site infections: A systematic review and meta-analysis of the literature, *BMJ Open*. 9 (2019), <https://doi.org/10.1136/bmjopen-2019-029727>.
- [23] D.J. Hess, M.J. Henry-Stanley, C.L. Wells, Gentamicin promotes staphylococcus aureus biofilms on silk suture, *Journal of Surgical Research*. 170 (2011) 302–308, <https://doi.org/10.1016/j.jss.2011.06.011>.
- [24] A. Hassoun, P.K. Linden, B. Friedman, Incidence, prevalence, and management of MRSA bacteremia across patient populations—a review of recent developments in MRSA management and treatment, *Crit Care*. 21 (2017) 211, <https://doi.org/10.1186/s13054-017-1801-3>.
- [25] T. Baygar, N. Sarac, A. Ugur, I.R. Karaca, Antimicrobial characteristics and biocompatibility of the surgical sutures coated with biosynthesized silver nanoparticles, *Bioorg Chem.* 86 (2019) 254–258, <https://doi.org/10.1016/j.bioorg.2018.12.034>.
- [26] S. Ferraris, S. Spriano, Antibacterial titanium surfaces for medical implants, *Materials Science and Engineering C*. 61 (2016) 965–978, <https://doi.org/10.1016/j.msec.2015.12.062>.
- [27] Y. Iwahashi, J. Wang, Z. Horita, M. Nemoto, T.G. Langdon, Principle of Equal-Channel Angular Pressing for the processing of ultra-fine grained materials, *Scr Mater.* 35 (1996) 143–146, <https://doi.org/10.1002/art.21843>.
- [28] ASTM E8, ASTM E8/E8M standard test methods for tension testing of metallic materials, *Annual Book of ASTM Standards* 4. (2010) 1–27. 10.1520/E0008.
- [29] ASTM G5–14. Standard Reference Test Method for Making Potentiodynamic Anodic Polarization Measurements, *Annual Book of ASTM Standards*. (2014). 10.1520/G0005–14.2.
- [30] ASTM G102–89, 2015. Standard Practice for Calculation of Corrosion Rates and Related Information from Electrochemical Measurements, *Annual Book of ASTM Standards*. (2015). 10.1520/G0102–89R15E01.2.
- [31] ASTM G31–72, 2004. Standard Practice for Laboratory Immersion Corrosion Testing of Metals, *Annual Book of ASTM Standards*. (2004). 10.1520/G0031–72R04.2.
- [32] *Iso 8407:2009., Corrosion of metals and alloys – Removal of corrosion products from corrosion test specimens*, International Organization for Standardization, 2009.
- [33] M. Sikora-Jasinska, E. Mostaied, A. Mostaied, R. Beanland, D. Mantovani, M. Vedani, Fabrication, mechanical properties and in vitro degradation behavior of newly developed Zn–Ag alloys for degradable implant applications, *Materials Science and Engineering C*. 77 (2017) 1170–1181, <https://doi.org/10.1016/j.msec.2017.04.023>.
- [34] G.K. Levy, J. Goldman, E. Aghion, The prospects of zinc as a structural material for biodegradable implants—a review paper, *Metals (Basel)*. 7 (2017) 1–18, <https://doi.org/10.3390/met7100402>.
- [35] K.B. Törne, Zn – Mg and Zn – Ag degradation mechanism under biologically relevant conditions, *Surf Innov.* (2017) 1–12.
- [36] Y.F. Zheng, X.N. Gu, F. Witte, Biodegradable metals, *Materials Science and Engineering R*. 77 (2014) 1–34, [https://doi.org/10.1007/978-1-4614-3942-4\\_5](https://doi.org/10.1007/978-1-4614-3942-4_5).
- [37] H. Li, Y. Zheng, L. Qin, Progress of biodegradable metals, *Progress in Natural Science: Materials International*. 24 (2014) 414–422, <https://doi.org/10.1016/j.pnsc.2014.08.014>.
- [38] H.S. Han, S. Loffredo, I. Jun, J. Edwards, Y.C. Kim, H.K. Seok, F. Witte, D. Mantovani, S. Glyn-Jones, Current status and outlook on the clinical translation of biodegradable metals, *Materials Today*. 23 (2019) 57–71, <https://doi.org/10.1016/j.mattod.2018.05.018>.
- [39] C. García-Mintegui, L.C. Córdoba, J. Buxadera-Palmero, A. Marquina, E. Jiménez-Piqué, M.P. Ginebra, J.L. Cortina, M. Pegueroles, Zn–Mg and Zn–Cu alloys for stenting applications: From nanoscale mechanical characterization to in vitro degradation and biocompatibility, *Bioact Mater.* 6 (2021) 4430–4446, <https://doi.org/10.1016/j.bioactmat.2021.04.015>.
- [40] D.W.Y. Toong, J.C.K. Ng, Y. Huang, P.E.H. Wong, H.L. Leo, S.S. Venkatraman, H.Y. Ang, Bioresorbable metals in cardiovascular stents: Material insights and progress, *Materialia (Oxf)*. 12 (2020), <https://doi.org/10.1016/j.mtl.2020.100727> 100727.
- [41] S. Prithivirajan, S. Narendranath, V. Desai, Analysing the combined effect of crystallographic orientation and grain refinement on mechanical properties and corrosion behaviour of ECAPed ZE41 Mg alloy, *Journal of Magnesium and Alloys*. 8 (2020) 1128–1143, <https://doi.org/10.1016/j.jma.2020.08.015>.
- [42] Z. Xu, H. Liu, K. Ren, C. Sun, X. Zhuo, K. Yan, J. Ju, F. Xue, J. Bai, J. Jiang, Revealing the abnormal softening mechanisms of Zn–xCu (x=2, 3) wrought alloys by gradually increasing ECAP numbers, *Materials Science and Engineering A*. 856 (2022), <https://doi.org/10.1016/j.msea.2022.143962>.
- [43] X. Yan, Q. Li, S. Yin, Z. Chen, R. Jenkins, C. Chen, J. Wang, W. Ma, R. Bolot, R. Lupoi, Z. Ren, H. Liao, M. Liu, Mechanical and in vitro study of an isotropic Ti6Al4V lattice structure fabricated using selective laser melting, *J Alloys Compd.* 782 (2019) 209–223, <https://doi.org/10.1016/j.jallcom.2018.12.220>.
- [44] L. Wang, J. Kang, C. Sun, D. Li, Y. Cao, Z. Jin, Mapping porous microstructures to yield desired mechanical properties for application in 3D printed bone scaffolds and orthopaedic implants, *Mater Des.* 133 (2017) 62–68, <https://doi.org/10.1016/j.matdes.2017.07.021>.
- [45] R. Hedayati, M. Sadighi, M. Mohammadi-Aghdam, A.A. Zadpoor, Analytical relationships for the mechanical properties of additively manufactured porous biomaterials based on octahedral unit cells, *Appl Math Model.* 46 (2017) 408–422, <https://doi.org/10.1016/j.apm.2017.01.076>.
- [46] J. Feng, B. Liu, Z. Lin, J. Fu, Isotropic octet-truss lattice structure design and anisotropy control strategies for implant application, *Mater Des.* 203 (2021), <https://doi.org/10.1016/j.matdes.2021.109595>.
- [47] S. Liu, D. Kent, H. Zhan, N. Doan, M. Dargusch, G. Wang, Dynamic recrystallization of pure zinc during high strain-rate compression at ambient temperature, *Materials Science and Engineering A*. 784 (2020), <https://doi.org/10.1016/j.msea.2020.139325> 139325.
- [48] K. Sztwiernia, J. Kawałko, M. Bieda, K. Berent, Microstructure of polycrystalline zinc subjected to plastic deformation by complex loading, *Archives of Metallurgy and Materials*. 58 (2013) 157–161, <https://doi.org/10.2478/V10172-012-0167-4>.
- [49] P. Tang, J. Feng, Z. Wan, X. Huang, S. Yang, L. Lu, X. Zhong, Influence of grain orientation on hardness anisotropy and dislocation behavior of AlN ceramic in nanoindentation, *Ceram Int.* 47 (2021) 20298–20309, <https://doi.org/10.1016/j.ceramint.2021.04.038>.
- [50] C.Y. Hu, X.L. Wan, Y.J. Zhang, X.T. Deng, Z.D. Wang, R.D.K. Misra, The synergistic effect of grain boundary and grain orientation on micro-mechanical properties of austenitic stainless steel, *J Mech Behav Biomed Mater.* 118 (2021), <https://doi.org/10.1016/j.jmbbm.2021.104473>.
- [51] S.Y. Betsofen, I.A. Grushin, M.I. Gordeeva, K.A. Speranskii, Inverse Pole Figures and the Anisotropy of the Properties of HCP Alloys, *Russian Metallurgy (Metally)*. 2022 (2022) 355–362, <https://doi.org/10.1134/S0036029522040048>.
- [52] T. Matsunaga, T. Kameyama, K. Takahashi, E. Sato, Constitutive relation for ambient-temperature creep in hexagonal close-packed metals, *Mater Trans.* 50 (2009) 2858–2864, <https://doi.org/10.2320/matertrans.M2009223>.
- [53] E. Mostaied, M. Hashempour, A. Fabrizi, D. Dellasega, M. Bestetti, F. Bonollo, M. Vedani, Microstructure, texture evolution, mechanical properties and corrosion behavior of ECAP processed ZK60 magnesium alloy for biodegradable applications, *J Mech Behav Biomed Mater.* 37 (2014) 307–322, <https://doi.org/10.1016/j.jmbbm.2014.05.024>.
- [54] E. Mostaied, A. Fabrizi, D. Dellasega, F. Bonollo, M. Vedani, Microstructure, mechanical behavior and low temperature superplasticity of ECAP processed ZM21 Mg alloy, *J Alloys Compd.* 638 (2015) 267–276, <https://doi.org/10.1016/j.jallcom.2015.03.029>.
- [55] W. Bednarczyk, J. Kawałko, B. Rutkowski, M. Wątroba, N. Gao, M.J. Starink, P. Bała, T.G. Langdon, Abnormal grain growth in a Zn–0.8Ag alloy after processing by high-pressure torsion, *Acta Mater.* 207 (2021). 10.1016/j.actamat.2021.116667.
- [56] B. Joseph, A. George, S. Gopi, N. Kalarikkal, S. Thomas, Polymer sutures for simultaneous wound healing and drug delivery – A review, *Int J Pharm.* 524 (2017) 454–466, <https://doi.org/10.1016/j.ijpharm.2017.03.041>.
- [57] K. van de Velde, P. Kiekens, Material Properties Biopolymers: overview of several properties and consequences on their applications, 2002. [www.elsevier.com/locate/polytest](http://www.elsevier.com/locate/polytest).
- [58] M. Asgari, R. Hang, C. Wang, Z. Yu, Z. Li, Y. Xiao, Biodegradable metallic wires in dental and orthopedic applications: A review, *Metals (Basel)*. 8 (2018) 1–32, <https://doi.org/10.3390/met8040212>.
- [59] P. jun Wang, L. wei Ma, X. qun Cheng, X. gang Li, Influence of grain refinement on the corrosion behavior of metallic materials: A review, *International Journal of Minerals, Metallurgy and Materials*. 28 (2021) 1112–1126, <https://doi.org/10.1007/s12613-021-2308-0>.
- [60] M.W. Vaughan, A.I. Karayan, A. Srivastava, B. Mansoor, J.M. Seitz, R. Eifler, I. Karaman, H. Castaneda, H.J. Maier, The effects of severe plastic deformation on the mechanical and corrosion characteristics of a bioresorbable Mg–ZKQX6000

- alloy, *Materials Science and Engineering C*. 115 (2020), <https://doi.org/10.1016/j.msec.2020.111130>.
- [61] K.L. Chang, T.C. Hung, B.S. Hsieh, Y.H. Chen, T.F. Chen, H.L. Cheng, Zinc at pharmacologic concentrations affects cytokine expression and induces apoptosis of human peripheral blood mononuclear cells, *Nutrition*. 22 (2006) 465–474, <https://doi.org/10.1016/j.nut.2005.11.009>.
- [62] N. Hadrup, A.K. Sharma, K. Loeschner, Toxicity of silver ions, metallic silver, and silver nanoparticle materials after in vivo dermal and mucosal surface exposure: A review, *Regulatory Toxicology and Pharmacology*. 98 (2018) 257–267, <https://doi.org/10.1016/j.yrtph.2018.08.007>.
- [63] A.B.G. Lansdown, A pharmacological and toxicological profile of silver as an antimicrobial agent in medical devices, *Adv Pharmacol Sci*. 2010 (2010), <https://doi.org/10.1155/2010/910686>.
- [64] R.J. Guillory, E. Mostaed, A.A. Oliver, L.M. Morath, E.J. Earley, K.L. Flom, T.M. Kolesar, A. Mostaed, H.D. Summers, M.P. Kweisa, J.W. Drellich, K.D. Carlson, D. Dragomir-Daescu, J. Goldman, Improved biocompatibility of Zn–Ag-based stent materials by microstructure refinement, *Acta Biomater.* (2022), <https://doi.org/10.1016/j.actbio.2022.03.047>.
- [65] D. L. Dunn, *Wound Closure Manual*, 2005.
- [66] T. Sun, H. Hao, W. ting Hao, S. min Yi, X. peng Li, J. rong Li., Preparation and antibacterial properties of titanium-doped ZnO from different zinc salts, *Nanoscale Res Lett*. 9 (2014) 1–11, <https://doi.org/10.1186/1556-276X-9-98>.
- [67] M. Roknian, A. Fattah-alhosseini, S.O. Gashti, M.K. Keshavarz, Study of the effect of ZnO nanoparticles addition to PEO coatings on pure titanium substrate: Microstructural analysis, antibacterial effect and corrosion behavior of coatings in Ringer's physiological solution, *J Alloys Compd.* 740 (2018) 330–345, <https://doi.org/10.1016/j.jallcom.2017.12.366>.
- [68] B. Abebe, E.A. Zereffa, A. Tadesse, H.C.A. Murthy, A Review on Enhancing the Antibacterial Activity of ZnO: Mechanisms and Microscopic Investigation, *Nanoscale Res Lett*. 15 (2020), <https://doi.org/10.1186/s11671-020-03418-6>.
- [69] E.M. Petrus, S. Tinakumari, L.C. Chai, A. Ubong, N. Chai, R. Son, A study on the minimum inhibitory concentration and minimum bactericidal concentration of Nano Colloidal Silver on food-borne pathogens, 2011.
- [70] P. Parvekar, J. Palaskar, S. Metgud, R. Maria, S. Dutta, The minimum inhibitory concentration (MIC) and minimum bactericidal concentration (MBC) of silver nanoparticles against *Staphylococcus aureus*, *Biomater Investig, Dent*. 7 (2020) 105–109, <https://doi.org/10.1080/26415275.2020.1796674>.
- [71] Y. Cheng, G. Feng, C.I. Moraru, Micro-and nanotopography sensitive bacterial attachment mechanisms: A review, *Front Microbiol*. 10 (2019), <https://doi.org/10.3389/fmicb.2019.00191>.
- [72] Y. Wang, A. Guan, I. Isayeva, K. Vorvolakos, S. Das, Z. Li, K.S. Phillips, Interactions of *Staphylococcus aureus* with ultrasoft hydrogel biomaterials, *Biomaterials*. 95 (2016) 74–85, <https://doi.org/10.1016/j.biomaterials.2016.04.005>.
- [73] K. Törne, M. Larsson, A. Norlin, J. Weissenrieder, Degradation of zinc in saline solutions, plasma, and whole blood, *J Biomed Mater Res B Appl Biomater*. 104 (2016) 1141–1151, <https://doi.org/10.1002/jbm.b.33458>.
- [74] K. Beausant Törne, A. Örnberg, J. Weissenrieder, Characterization of the protective layer formed on zinc in whole blood, *Electrochim Acta*. 258 (2017) 1476–1483, <https://doi.org/10.1016/j.electacta.2017.12.018>.
- [75] M. Sikora-Jasinska, J. Goldman, E. Mostaed, J.W. Drellich, Albumins inhibit the corrosion of absorbable Zn alloys at initial stages of degradation, *Surf Innov*. 8 (2020) 234–249, <https://doi.org/10.1680/jsuin.19.00063>.
- [76] A.A. Barros, C. Oliveira, E. Lima, A.R.C. Duarte, K. Healy, R.L. Reis, 7.41 Ureteral stents technology: Biodegradable and drug-eluting perspective, in: *Comprehensive Biomaterials II*, Elsevier, 2017: pp. 793–812. 10.1016/B978-0-12-803581-8.10189-4.